

3D seismic characterization of a complex sediment drift in the South China Sea: evidence for unsteady flow regime

Qiliang Sun^{a,b,*}, Joe Cartwright^c, Thomas Lüdmann^d, Shiguo Wu^e, Genshun Yao^f,

^a*Key Laboratory of Tectonics and Petroleum Resources of Ministry of Education, Faculty of
Resources, China University of Geosciences, Wuhan 430074, China;*

^b*Department of Marine Science and Engineering, Faculty of Resources, China University of
Geosciences, Wuhan 430074, China;*

^c*Department of Earth Sciences, University of Oxford, Oxford OX1 3AN, England;*

^d*Department of Geosciences, Centre for Earth System Research and Sustainability, University of
Hamburg, Hamburg, Germany;*

^e*Sanya Institute of Deep-sea Science and Engineering, Chinese Academy of Sciences, Sanya
572000, China;*

^f*PetroChina Hangzhou Institute of Geology, Hangzhou 310023, China*

Abstract

This study describes a previously unobserved reflection seismic configuration comprising a honeycomb planform and a repeated erosion/infill cross section, based on high-resolution 3D/2D seismic data and bathymetric data. The honeycomb structures cover an area of more than 5,000 km² and are developed within the Late Miocene to Recent deep-water sediments of the northwestern South China Sea. Linear erosional troughs up to 10 km long and 1 km wide are

*Corresponding author. Tel.: +84 053282898872; fax: +84 0532 8289 8544.
E-mail address: sunqiliang@cug.edu.cn.

widely developed in this area, are intimately related to the particular seismic configuration, and interpreted to represent a new type of sediment drift that is caused by unsteady bottom current regimes operative since the Late Miocene. The unsteady bottom current regimes are suggested to be triggered by irregular seabed morphologies. Considerable seafloor topography was generated as a direct result of tectonic movements in the area since the Late Miocene, and this topography then influenced the pathway of strong bottom currents. This study highlights that: (1) an unsteady bottom current regime can be laterally extensive and persist for millions of years; (2) structurally controlled seafloor relief plays an important role in controlling the depositional pattern; and (3) the bottom currents were active since the Late Miocene, flowing from southeast through the Xisha-Guangle Gateway and crossing the honeycomb structure zone. This study documents a new style of drift and will help to improve our knowledge of paleoceanography and our understanding of the South China Sea (SCS) deep-water circulation which is at present still poorly understood.

Keywords

Contourite drift, bottom current, unsteady flow system, paleoceanography, honeycomb structures, South China Sea

1. Introduction

Bottom current deposition has been widely studied for half a century or more (e.g. [Heezen and Hollister, 1964](#); [Faugères et al., 1999](#); [Rebesco et al., 2014](#)), but the influence of bottom current circulation on deep-water sedimentary systems remains poorly understood ([Rebesco et al., 2014](#)). In the past two decades, knowledge of contourite depositional systems has grown quickly, because of their important implications for paleoceanography/paleoclimatology,

slope-stability/geological hazard assessment, and for hydrocarbon exploration (e.g. [Faugères et al., 1999](#); [Hernández-Molina et al., 2008](#); [Stow et al., 2009](#); [Lüdmann et al., 2012](#); [Rebesco et al., 2014](#); [Wang et al., 2014](#); [Hernández-Molina et al., 2014](#)). The extensive use of high-resolution 3D seismic data, 2D seismic data, multibeam bathymetrical data, and underwater video has led to significant improvements in the characterization of contourite deposits and their physical sedimentology (e.g. [Knutz and Cartwright, 2003](#); [Rebesco, 2005](#); [Hernández-Molina et al., 2008](#); [Stow et al., 2013](#)). Many different types of contourite drifts have been described from continental margin or abyssal settings ([Fig. 1a-g](#)) and they are nearly all interpreted as being deposited by stable bottom currents that persist for considerable periods of time ([Faugères et al., 1999](#)). However, in this study, we present evidence for a previously undescribed type of drift deposit with a highly unusual internal structure and planform morphology that we interpret as evidence for the action of unsteady bottom currents.

The internal structure or ‘architecture’ of this drift is extremely complex with repeated episodes of erosion and deposition expressed in km-scale, circular to elliptical, cut and fill structures. It has only been possible to recognise this intricate alternation of erosion and deposition with the benefit of high resolution 3D seismic data. One of the defining characteristics of this new type of drift architecture is that many of the bedforms and erosional discontinuities have an elliptical to circular planform. This study therefore aims to describe the detailed characteristics of this complex configuration, to interpret the physical processes responsible for this architecture, and to place the drift body in a wider paleoceanographic context such that similar phenomena may be more easily recognised on seismic data elsewhere.

2. Geological and oceanographic settings

2.1 Geological setting

The study area is located in the northwestern part of SCS, and includes the southern slope of the Qiongdongnan Basin (QDNB), the Guangle Massif (GLM) and the western part of Xisha Massif (XSM) (Fig. 2). The available database for this study covers an area of ca. 16,500 km², spanning a water depth range of 400 m to 1400 m. Focus of this study is the southern slope of QDNB (to the north of GLM), the region where the main drift body occurs (Fig. 3).

The QDNB belongs to the northern passive margin of the SCS. It was formed by lithospheric stretching during the Paleogene (rift stage), followed by thermal subsidence since the Miocene (post-rift stage) (Li et al., 1998). Faults mainly deform the rift succession and are rarely observed within the Neogene strata (Xie et al., 2006). However, polygonal faults are widely developed within the Late Miocene in the study and adjacent areas, suggesting that the faulted units are predominately fine-grained sediments (Sun et al., 2010).

The syn-rift succession is characterized by terrestrial sediments, such as alluvial and lacustrine deposits (Gong and Li, 1997). Marine deposition in the study area initiated in the Early Miocene (Ma et al., 2011). Shallow-water reefs and carbonate platforms developed on top of the two massifs (GLM and XSM) and in adjacent areas in the Early-Middle Miocene stages (Ma et al., 2011). Subsequently, the study area subsided and water depth dramatically increased (Xie et al., 2006). Two main sediment sources, the South China Block and the Indochina, were active in supplying sediment to the area in the Late Miocene and Pliocene (Yao et al., 2008). Large sediment fluxes sourced from the South China Block were deposited in the central and northern QDNB during the Quaternary (Wang et al., 2013). However, only a thin Quaternary drape

occurred at the southern part of the QDNB (Sun et al., 2011a). Small-scale cyclic deposition of channel-levee systems and mass transport deposits can be observed within the Quaternary strata to the west of the study area (Yuan et al., 2009; Sun et al., 2011a; Wang et al., 2013).

The Xisha Massif (XSM) is a separate mini-block caused by Cenozoic rifting (Taylor and Hayes, 1983) and has been suggested to have originated from the South China Block based on wide-angle seismic profiles and heat flow measurements (Fig. 2) (Qiu et al., 2001). The XSM has been in evidence since the rift stage and represents a paleo-high (Qiu et al., 2001). Likewise, the Guangle Massif (GLM) is a paleo-basement high, already existing prior to the Neogene (Fyhn et al., 2009). The GLM is separated from the Indochina Block through a narrow but very deep intra-basinal depression (Fig. 2) (Fyhn et al., 2009). It is located in the southwest part of the study area, trending NE-SW. The GLM lies at present water depth of ca. 400 m, standing above the surrounding seabed by 200 - 400 m (Fig. 3a). Pockmarks are widespread to the east and south of GLM and they are related to the underlying focused fluid flow structures (Sun et al., 2011b, 2013). They are tens of meters to several-kilometres in size and are circular, elliptical or crescentic in plan view (Sun et al., 2013). One large seamount, here named SM, is located to the east of GLM with exposed relief of 700 m above the seafloor (Fig. 3a). In all, the study area is located distally with respect to both the shelves and slopes of the South China Block and the Indochina Block (Fig. 2). It is in a structurally complex zone characterized by the bending of the Red River Fault Zone (RRFZ) which represents one of the major tectonic lineaments in Southeast Asia and changed its movement direction to right-lateral from 5.5 Ma (surface T30) onwards (Morley, 2002).

2.2 Oceanographic setting

Paleoceanographic investigations of the South China Sea (SCS) have intensified in the last 20

years (Wang et al., 2014), particularly in the northeastern SCS (e.g. Yuan, 2002; Lüdmann et al., 2005) where it is understood that ocean circulation is mainly controlled by its physiographic characteristics (Xie et al., 2013). No previous oceanographic or palaeoceanographic studies have been undertaken in the study area in the northwestern SCS, and its modern current regime is largely unknown.

The SCS is presently connected to the open ocean only through five straits (Hall, 2002) (Fig. 2) and the present circulation of the SCS is comprised of surface circulation (less than 350 m), intermediate circulation (350 m - 1350 m) and deep circulation (more than 1350 m) (e.g. Yuan, 2002; Chen et al., 2014; Wang et al., 2014). The surface circulation is southwestward in winter and reverses to northeast in summer, which is dominantly controlled by the East Asia monsoon system (e.g. Lüdmann et al., 2005). The intermediate circulation is anti-cyclonic (e.g. Yuan, 2002), is active over the continental slope of the Pearl River Mouth margin and is involved in the formation of unidirectionally migrating deep-water channels (Gong et al., 2013). The deep circulation is cyclonic and controlled by the 2600 m Luzon Strait sill which is the main gateway between the semi-closed SCS and the Pacific Ocean and through which the North Pacific Ocean and North Pacific Deep Water intrude into the SCS (Fig. 2) (Lüdmann et al., 2005).

3. Data and methods

The primary data source of this study is industrially acquired 3D and 2D reflection seismic and multibeam bathymetric data. The 3D seismic dataset covers an area of ca. 2,800 km² and has CDP (common depth point) distance and line spacing of 12.5 m and 25 m, respectively. The dominant frequency for the intervals of interest is 40-60 Hz, yielding a vertical seismic resolution of 8 -11 m

based on an average seismic velocity of 1750 m/s calibrated from borehole YC35-1-2 (Fig. 2). The 2D seismic dataset comprises more than 12,000 line kilometres, with a dominant frequency of ca. 35 Hz and a CMP (common middle point) interval of 6.25 and 12.5 m. The 2D seismic data has a vertical seismic resolution of ca. 13 m in the target intervals. The multibeam data has a lateral resolution of 100 m (cell size) and a vertical resolution of 1 m - 3.3 m (1% of the water depth). There are no wells located in the study area itself. However, the ages of the sequence boundaries, e.g. T40 (10.5 Ma), T30 (5.5 Ma) and T20 (1.9 Ma), were calibrated by correlation with nannofossil biostratigraphy obtained from nearby boreholes (e.g. YC35-1-2, LS2-1) to the north of the study area (Fig. 2).

The standard interpretation workflow for the detection, description and analysis of the seismic reflection configurations and amplitude anomalies involved a systematic examination of the seismic data using coherence and azimuth volumes, and 3D visualization, and was based on similar approaches adopted by Knutz and Cartwright (2004) and Hohbein and Cartwright (2006).

4. Results

4.1 Seismic stratigraphic interpretation

This study focuses on the uppermost 1-2 km of the sedimentary fill of the basin. This section is subdivided into four units based upon seismic configuration, seismic reflection amplitude, continuity and terminations (Figs. 4-8).

Unit 1 is composed of Late Miocene strata and is bounded between surfaces T40 and T30 (Fig. 4). The stratal thickness is variable across the study area and becomes thinner towards to the GLM (Fig. 4a). Unit 1 is deformed by closely spaced polygonal faults (Sun et al., 2010). Its seismic

154 reflections are parallel and continuous and can be traced regionally (Figs. 4-5).

155 Unit 2 is bounded between surfaces T30 and T20 and is assigned to the Pliocene. It consists of
156 variable amplitude seismic reflections and exhibits a highly complex internal configuration (Figs.
157 4-5). In the vertically exaggerated seismic profiles, Unit 2 appears to be composed of short and
158 discontinuous seismic reflections (Fig. 4). However, at true-scale display they appear as
159 undulating reflections with a wave-like morphology, complex seismic truncations, onlaps and
160 drapes (Figs. 5a-b). Towards to the north and west, these complex internal structures grade
161 laterally into well-stratified reflections (Fig. 4). The thickness of Unit 2 becomes thinner towards
162 to the SM (Fig. 4). Several linear erosional features (referred to here as 'troughs') are observed at
163 surface T30, and demarcated by truncated reflections of Unit 1 at their boundaries.

164 Unit 3 and Unit 4 are assigned to the Quaternary. Unit 3 is bounded by surfaces T20 and T10.
165 Compared with Unit 2, Unit 3 is characterized by nearly parallel, wave-like seismic reflections
166 (Figs. 5b-c). In the vertically exaggerated seismic profiles, the wave-like structures display a form
167 of trough-ridge configurations (Fig. 4). Discontinuous or onlap reflections can be also observed
168 within some troughs in Unit 3 (Figs. 5a-b). The seismic patterns of Unit 3 are less complex and
169 cover a smaller area than those of Unit 2 (Fig. 4a). Unit 3 is well-stratified and continuous
170 towards to the north (lower slope).

171 Unit 4 thickens toward the north (lower slope) in contrast to uniformly thin development in its
172 southern extent (Fig. 4a). In the northern region, Unit 4 onlaps onto Unit 3 and comprises
173 well-stratified seismic reflections (Figs. 4a, 5a). In the South, Unit 4 has a similar seismic
174 reflection pattern to Unit 3 and the configuration of Unit 4 mimics those of Unit 3 (Fig. 4).

4.1 Geomorphologic characteristics

The morphology of the present seabed and in the shallow subsurface in the study area is very complex. Most strikingly the region is dominated by a closely packed set of depressions whose geometrical arrangement is reminiscent of honeycomb structures, and we adopt this informal descriptive term in the following descriptive sections. In addition, the area contains numerous linear erosional troughs, deepwater channels, seamounts and structural massifs (Fig. 3).

4.1.1 Honeycomb structures

The honeycomb structures are kilometre scale features (Table 1) packed into a dense tessellation, and mainly occur in the southern sector of the Qiongdongnan Basin (to the north of the Guangle Massif), covering an area of ca. 5,000 km² (Fig. 3a). The erosional margins that define individual structures within the more complex tessellated pattern exhibit circular to irregular shapes in planform, and they have flat to undulatory bases and steep flanks of 2°-13° (Table. 1; Figs. 3e-f). They are usually asymmetric and their southwestern/southern sides are steeper and higher than their opposing sides (Fig. 6b). Some honeycomb structures are linked together and compose a composite structure. To the north and east, the zone of honeycomb structures abruptly passes over to the undisturbed seabed and there is a relief of 20-60 m between the two areas (Figs. 3a, 3e, 6a).

Unit 3 and Unit 4 have a similar depositional pattern with internal reflection configurations characterized by a wave-like cross-sectional structure with a honeycomb planform (Figs. 5-6a). In contrast, Unit 2 has a more complex depositional pattern (Fig. 7), with evidence of repeated erosion and infill (Figs. 8c, 8d) and denser honeycomb structures in planform (Fig. 7). Seismic truncations frequently occur against the closely spaced, concave erosional surfaces, and the

seismic reflections are highly discontinuous on a scale of less than a kilometer (Figs. 8c, 8d). All honeycomb structures within Unit 3 and Unit 4 originate from their small counterparts at the surface of T20 and their geometry mimics the depositional pattern of Unit 2 but at a larger scale (Fig. 7).

4.1.2 Main Channel

The Main Channel is a major linear, NW-SE oriented erosional depression at the modern seafloor, located in the southwest of the study area (Fig. 3a). This impressive feature becomes less erosive towards the NW, dying out within the honeycomb structure zone to the north (Fig. 3). The Main Channel is positioned along the western side of a basement high (topographic high) (Fig. 4b) and its steep NE flank owes its geometry to the underlying deformation associated with this basement structure (Fig. 5e). Chaotic seismic reflections are observed in the upper channel fill (Fig. 5e).

4.1.3 Troughs

The troughs are developed as a series of regularly spaced, mainly parallel erosional features at the southern and western flanks of the triangular shaped seamount (SM), where they are oriented parallel to the margins of this large topographic feature. They terminate fairly abruptly towards the east where honeycomb structures are found instead (Fig. 3b). Repeated erosion and infill structures can be observed within the sediments west of the trough (Figs. 4b, 5b-c).

Two groups of troughs are observed along the surface T30 (Figs. 4a, 8-9). One group is mainly located in the southern and eastern part of the 3D seismic survey where they have a similar orientation (NW-SE) to the Main Channel and to similar sized troughs observed at the present

seabed (Figs. 3a-b). The other more striking group is located in the northwestern part (Fig. 9a).

Both groups of troughs are ca. 1 km wide and linear. A few larger troughs erode downwards to T40 (Table. 1; Figs. 8a, 8d, 9b). The troughs are filled by Unit 2, with onlap onto their flanks. The bases of the troughs are undulating, and bifurcations or merging of some troughs are also observed. To the east, the interval with complex internal architecture grades laterally into undisturbed layers (Fig. 9a).

Many troughs are also observed along the surface of T20 (Fig. 10), but they are smaller than those developed at surface T30 (Table 1). These troughs have an orientation of NW-SE (Figs. 10, 11c). Bifurcations and merging of troughs are also observed and the troughs are connected with or terminate into the honeycomb structures along the surface of T20 (Fig. 10). The fill is characterized by a mixture of onlap and drape (Fig. 10b).

The sequence boundaries T20 and T30 can be correlated and mapped relatively easily, but it is difficult to trace any mappable, continuous horizon within the complex reflection configurations of Unit 2 because of the intensity of the cut and fill geometries. Instead, four coherence slices are presented to show the internal structures of the units (Unit 1 – Unit 3) (Fig. 11). Linear troughs which have similar characteristics with these along surface T20 (e.g. the NW-SE extension) occur together with honeycomb structures in Unit 3 (Fig. 11a). Linear troughs can be clearly identified in the coherence slice between the top of Unit 2 and base of Unit 3 (Fig. 11b). They maintain a WNW-ESE trend. Two groups of troughs can be observed within the Unit 2 (Fig. 11c). One has an E-W strike and the other strikes NW-SE. Likewise, in the lower part of Unit 2 and upper part of Unit 1, troughs can be subdivided into two groups (Fig. 11d). The NW-SE oriented troughs dominate the lower part of Unit 2 and the E-W oriented troughs mainly develop at the

northwestern part of the study area.

4.1.3 Xisha-Guangle Gateway

The Xisha-Guangle Gateway (XGG) is located between the Xisha Massif and Guangle Massif (Fig. 3). It is a deep, narrow, straight and strait-like pathway. The XGG is ca. 130 km long and 15-20 km wide with a depth of ca. 100-180 m (Figs. 3a, 3d). It is aligned SE to NW and has a flat seabed which shallows from the center to both the NW and SE. There are numerous small-scale linear troughs locating mainly at the western flank of XGG and having a similar strike direction relative to the XGG (from NW to SE) (Fig. 3a).

4.4 Anticlinal basement structures

Using the 2D and 3D seismic data, we mapped a number of distinct buried positive tectonic structures in the study area (Fig. 4b, 12-13). They are manifested by elongated ridge-like features with different orientations and extent that do not reach the seafloor (Fig. 12). The area of honeycomb structures of Units 2 to 4, especially Unit 2, is approximately encompassed by these tectonic structures. The western boundary is characterized by an N-S elongated anticlinal structures (basement highs) ca. 15 km in width that pinches out into the central subsidence zone belonging to the QDNB (Fig. 12). The eastern boundary is approximately marked by an N-S to NNW orientated anticlinal structure that terminates in the southeastern corner of the 3D study area. This structure is ca. 25 km wide in the south and tapers towards the NNW (Fig. 12). In the north, the strike of the anticlinal structures is SE-NW and terminates within the central subsidence zone (Fig. 12). Moreover, there are also some small-scale isolated anticlinal structures developing under the honeycomb structure units (Figs. 12-13).

Most of these structural highs deform the sedimentary column up to and including Unit 3 and

must therefore have developed before the deposition of Unit 4 (Fig. 4b). Only in a small area does the anticlinal structure continue to be expressed into the modern seafloor, leading to the folding of the youngest parts of Unit 4 (Fig. 4b). On top of the uplifts the sedimentary cover is disrupted and faults developed that mostly terminate at T40. However, some of them continue within Unit 2 and Unit 3 (Fig. 4b), but none reaches Unit 4.

5. Discussion

5.1 Physical explanation for the observed seismic pattern

To our knowledge, the seismic features observed in the course of our investigation have not been described in any previous study. Units 2, 3 and 4 consist of the same complex seismic facies, which are characterized by circular to sub-circular depressions in planform (Fig. 7). Importantly, Unit 3 and Unit 4 can be seen to mimic the underlying planform pattern established within Unit 2. Unit 2 is therefore the key to understanding the origin of the complex structures in the study area.

An origin of the honeycomb structures as large-scale mass transport deposits was considered as one possible explanation of the observed strata geometries. However, we do not observe any linear features typical of mass transport deposits such as headwalls or lateral scarps, extension updip, or compression downdip in the the headwall or toe domains, respectively (e.g. Bull et al., 2009). Although the observed structures are wave-like, our 3D seismic and bathymetric data clearly demonstrates their concentric shape (Figs. 3a, 6). This indicates that the lateral movement of the sediments is limited and mass wasting (if any) is not the main cause for the origin of the honeycomb structures. A pockmark origin was also considered, but is easily rejected based on

the lack of any seismic evidence for fluid flow pathways underneath the honeycomb structures (Figs. 8a, 8d). Moreover, pockmarks tend to have smoothly curving perimeters (Judd and Hovland, 2007), and are commonly circular to subcircular, in contrast to the honeycomb geometry observed here.

The detailed seismic features, especially the repeated erosion and infill (e.g. Figs. 8c, 8f), instead point to a physical mechanism in which these structures are caused by unsteady currents. Three possible candidates for the current regime leading to this complex architecture are considered here, namely: (1) turbidity currents, (2) bottom-water currents and (3) a combination of the former two currents. Repeated erosion and infill are usually observed in confined deep-water channels and submarine canyons (e.g. Stow and Johansson, 2000; Clark and Cartwright, 2011; Gong et al., 2013), but such a 'honeycomb' geometry in planform associated with these confined channels and canyons has never been observed. Moreover, the study area and its environs were fully established as a deep marine setting during the deposition of Unit 2 (Gong and Li, 1997; Sun et al., 2010) and were distal from the shelf making a direct source from downslope transport very improbable. Deep-water turbidity channels are observed but only in the form of the channel-levee complexes of Unit 4 (Yuan et al., 2009; Sun et al., 2011a) as observed at the present seabed and are not seen within the complex strata of Unit 2 - Unit 3. This further suggests that turbidity currents have at most a minor role in the formation of these complex seismic patterns.

The present seabed geomorphology suggests that strong bottom currents occur in the study area, as evidenced by the following main observations:

(1) The Main Channel extends along the eastern foot of GLM and straight extends downslope

to its end (Fig. 3a).

(2) The linear troughs flanking the SM are directly comparable in dimension, cross-section, and planform with erosional/depositional features or 'moats' that are commonly documented in bottom current regimes where there is an influence of topography, along topographic highs, such as ridges, banks and islands worldwide (e.g. Faugères et al., 1999; Knutz and Cartwright, 2003; Laberg et al., 2007; Suriyk and Lykke-Andersen, 2007; Hernández-Molina et al., 2008; Van Rooij et al., 2009; Faugères and Mulder, 2011). Similar erosional troughs formed by bottom currents are also documented in many present and ancient continental margins, such as in the Gulf of Cadiz (Hernández-Molina et al., 2006), the Faeroe-Shetland gateway (Knutz and Cartwright, 2003), the Northwest Sub-basin of SCS (Chen et al., 2014) and the Pearl River Mouth Basin of northern SCS (Sun et al., 2016).

(3) The elliptical and crescentic mega-pockmarks in the adjacent area also indicate strong bottom current occur in the study area (Sun et al., 2011b) by analogy with similar structures such as, in the Inner Oslofjord, Norway (Hammer et al., 2009) and Adriatic Margin (Verdicchio and Trincardi, 2006).

By analogy with the modern seabed, it is also argued that strong bottom currents were the dominant influence at earlier periods within the Neogene. A number of troughs which have strikes of NW-SE or W-E also occurred within Units 2-3 (Figs. 9-11). These troughs have almost identical characteristics with those occurring at the present seabed, which indicates they probably have a similar origin, i.e. strong bottom currents. All these observations and comparisons suggest that strong bottom currents have probably been active in the study area since the Late Miocene.

5.2 Controlling factors and current flow regimes

5.2.1 Controlling factors

Contourite drifts having different morphologies and configurations occur in contrasting settings of basin floors, slopes and shelves and are usually formed by long-lived stable current flow regimes (e.g. [Faugères et al., 1999](#); [Niemi et al., 2000](#); [Stow et al., 2013](#); [Rebesco et al., 2014](#)). Such drifts are well studied and usually have large dimensions (10s of kilometres length scale). Small-scale unsteady current flow regimes have been previously reported from regions close to topographic features such as seamounts, ridges, straits, mounds, banks and canyons as referred above (e.g. [Roberts et al., 1974](#); [Faugères et al., 1999](#); [Masson et al., 2004](#); [Hernández-Molina et al., 2006](#); [Rebesco et al., 2014](#)), and consequently, small-scale cut and fill patterns were usually observed associated with these topographic features ([Faugères et al., 1999](#); [Rebesco et al., 2014](#)). However, it has not previously been suggested that a single drift body of the scale shown here could have been formed by an unsteady flow regime.

The occurrence of strong unstable bottom currents is most likely attributed to the complex seabed morphologies ([Fig. 13](#)). As noted above, tectonic derived highs, especially boundary anticlinal structures and seamounts are widely distributed in the study area ([Figs. 4, 12-13](#)). The uplifted regions deform the sedimentary column up to, and including Unit 3, implying that crustal scale deformation must have preceded the deposition of Unit 4. The local tectonic uplift of strata is attributed to the reversal of Red River Fault Zone (RRFZ) which changed its movement direction from left-lateral to right-lateral since 5.5 Ma (Surface T30) onwards and earthquakes frequently occurred during the uplifting phases ([Morley, 2002](#)). The uplift not only makes the seabed

uneven, but also disrupts the entire sediment package, which results in extensional stress directly above the anticlinal structures and compression within the adjacent lows (Figs. 4, 12). As a result, faults have developed above the anticlinal structures (basement highs) and small-scale gravitational gliding was possibly evoked (Fig. 4b, frame a). The basement highs themselves, and associated small-scale sediment creep caused by uplift, probably contribute to the uneven seabed morphologies.

The GLM and XSM could have acted like partially confining walls and obstructed the normal flow of bottom current, leaving just a narrow 'tectonic' gateway for bottom currents to pass through, similar to bottom currents flowing through straits such as the Gibraltar Strait (e.g. Hernández-Molina et al., 2006) and the Denmark Strait (e.g. Karcher et al., 2011). Strong bottom currents would have flowed into the study area and impinged upon and interacted with the complex seabed morphologies, which would in turn have disrupted the flows and made them more unsteady or erratic. Moreover, the honeycomb structure zone of Unit 2 is bounded by the linear anticlinal structures (basement highs) to the north and to the west as referred above (Fig. 12). These linear structures would have confined the bottom currents and restricted their flows, resulting in an amplification if any instability in the current regime. In summary, we suggest that the tectonically controlled complex paleo-seabed morphologies probably promoted and fostered the unstable bottom currents and resulted in this particular form of sediment drift. In the Quaternary, along with the increase of sediment supply and the weaker activities of RRFZ, the uneven seabed was filled and the honeycomb structures were buried by the sediments from the northern sources, just like those observed in the northern part of the study area (Figs. 4a, 8a, 8d).

Besides the complex seabed morphologies, the downslope effect of bottom currents possibly

also contributed to the formation and preservation of honeycomb structures. Most documented bottom currents flow along the bathymetric contours of continental slopes or topographic highs, such as continental banks, ridges and seamounts (e.g. [Faugères et al., 1999](#); [Knutz and Cartwright, 2003](#); [Hernández-Molina et al., 2006](#); [Van Rooij et al., 2009](#)). However, the troughs at the surface of T30 which have the same strikes with the present seabed Main Channel indicate that the paleo-bottom current, just like their present counterpart, flowed mainly downslope not alongslope ([Fig. 3](#)). The bottom currents would split the flow into two or more cores and branches when they flow downwards along a varying bottom slope ([Serra et al., 2010](#)). In this case, the flows are nearly always unstable and they would break up into a train of eddies ([Sutherland et al., 2004](#)). This could cause the formation of a number of depressions on the seabed, such as honeycomb structures as documented in our study and analogous too, with those modeled at the outflow area of the Red Sea ([Nof et al., 2002](#)).

5.2.2 Current flow regime

The seabed morphologies caused by bottom currents can be used to infer the nature of the prevailing flow regimes (e.g. [Stow et al., 2009](#)). The occurrence of the troughs/moats along the western slopes of the SM, and the Main Channel and the XGG extending to the NW suggest that the present bottom currents flow NW through the XGG ([Fig. 3](#)). The widespread development of NW-SE troughs in Unit 2 (Late Miocene) indicate that the bottom currents in the Late Miocene possibly had a similar flow pattern analog to the present day regime, i.e., the bottom currents from XGG (Xisha-Guangle Gateway) dominate in the study area ([Fig. 9](#)). However, the bottom currents flowing from W to E gradually gained in influence in the study area ([Figs. 11a-b, 13b](#)). Together, this combination of bottom currents and the sediment sources are suggested to be the

main factors controlling the deposition of the study area during Unit 3 (Pliocene). In the Quaternary, a huge flux of terrigenous sediments from northern sources was transported into the study area and covered the northern part of Unit 4 (Figs. 4a, 8a, 8d).

5.3 Implications

Bottom current processes are operative to some extent almost everywhere in the oceans and slopes, and are important for shaping the seafloor and controlling deep-water deposition (e.g. Stow et al., 2009; Knutz and Cartwright, 2003; Hernández-Molina et al., 2006; Van Rooij et al., 2009; Gong et al., 2013). Here we describe a new type of drift body whose characteristic honeycomb structure is suggested to be caused by unstable bottom currents. The similar seismic patterns (honeycomb structures in plan view and repeated erosions and infills in vertical profiles) are also observed in the northern part of Xisha Massif and Pearl River Mouth Basin of northern South China Sea, based on high-resolution 3D seismic and bathymetric data, so these ‘unsteady’ drifts may be more widespread in the SCS. It seems reasonable to expect that similar seismic patterns should occur more widely worldwide (such as gateway, strait and seabed with complex morphologies), where structurally controlled topography occurs at the appropriate scale relative to the flow regime, such that a normally steady flow pattern is disrupted in the manner we suggest here. They may well be more frequently observed as in future as high-resolution 3D seismic data and bathymetric data are more widely available for research purposes.

6. Conclusions

1. A new type of sediment drift is defined that is characterized by cut and fill erosional features

with a honeycomb planform and is mapped over a large area in the northwestern part of South China Sea.

2. This sediment drift is attributed to the actions of the unsteady flow system of bottom currents initiated in the Late Miocene and active until the present day.
3. The origin of unsteady bottom current flows is most likely caused by the uneven seabed morphologies which were triggered by basement uplifting. Besides the complex morphologies of the seabed, the downslope flow of bottom currents also contributed to the formation of this sedimentary pattern.
4. This study highlights that the unsteady current regimes could occur at a large scale, e.g. more than 5,000 km² and more cases could be observed through the widespread usage of high-resolution 3D seismic data and bathymetrical data.

Acknowledgements

This work was supported by the National Scientific Foundation of China (Grant No. 41306054, 41372112, 91228208), the National Basic Research Program of China (2015CB251201). We thank Chief Editor Nigel Mountney, Associate Editor Jess Trofimovs, Reviewer Ian Kane and an anonymous reviewer for their constructive comments which greatly improve this manuscript. The China National Petroleum Company is thanked for permission to release these data. The authors are also grateful to Dr. Duanxin Chen and Yintao Lu for their fruitful discussions.

References

- Andresen, K.J. and Huuse, M. (2011) 'Bulls-eye' pockmarks and polygonal faulting in the Lower Congo Basin: relative timing and implications for fluid expulsion during shallow burial. *Marine Geology*, **279**, 111–127.

440 Bull, S., Cartwright, J. and Huuse, M. (2009) A review of kinematic indicators from mass-transport
 441 complexes using 3D seismic data. *Marine and Petroleum Geology*, **26**, 1132-1151.

442 Chen, H., Xie, X.N., Van Rooij, D., Vandorpe, T., Su, M. and Wang, D.X. (2014) Depositional
 443 characteristics and processes of alongslope currents related to a seamount on the
 444 northwestern margin of the Northwest Sub-Basin, South China Sea. *Marine Geology*, **355**,
 445 36-53.

446 Clark, I. R. and Cartwright, J. A. (2011) Key controls on submarine channel development in
 447 structurally active settings. *Marine and Petroleum Geology*, **28**, 1333-1349.

448 Faugères, J. C. and Mulder, T. (2011) Contour currents and contourite drifts. In: *Deep-sea*
 449 *Sediments. Developments in Sedimentology* (Eds Hüneke, H and T, Mulder), 63, pp. 149–214.
 450 Elsevier, Amsterdam.

451 Faugères, J.C., Stow, D.A.V., Imbert, P. and Viana, A.R. (1999) Seismic features diagnostic of
 452 contourite drifts. *Marine Geology*, **162**, 1–38.

453 Fyhn, M.B.W., Boldreel, L.O. and Nielsen, L.H. (2009) Geological development of the Central and
 454 South Vietnamese margin: implications for the establishment of the South China Sea,
 455 Indochinese escape tectonics and Cenozoic volcanism. *Tectonophysics*, **478**, 184–214.

456 Gong, C.L., Wang, Y.M., Zhu, W.L., Li, W.G. and Xu, Q. (2013). Upper Miocene to Quaternary
 457 unidirectionally migrating deep-water channels in the Pearl River Mouth Basin, northern South
 458 China Sea. *AAPG Bulletin*, **97**, 285–308.

459 Gong, Z.S. and Li, S.T. (1997) Continental margin basin analysis and hydrocarbon accumulation of
 460 the Northern South China Sea. Science Press, Beijing, 356 pp.

461 Hammer, O., Webb, K.E. and Depreiter, D. (2009) Numerical simulation of upwelling currents in

462 pockmarks, and data from the Inner Oslofjord, Norway. *Geo-Marine Letters*, **29**, 269-275.

463 Heezen, B.C. and Hollister, C.D. (1964) Deep sea current evidence from abyssal sediments.

464 *Marine Geology*, **1**, 141–174.

465 Hernández-Molina, F.J., Llave, E., Stow, D.A.V., Garcia, M., Somoza, L., Vazquez, J.T., Lobo, F.J.,

466 Maestro, A., Del Rio, V.D., Leon, R., Medialdea, T. and Gardner, J. (2006) The contourite

467 depositional system of the Gulf of Cadiz: a sedimentary model related to the bottom current

468 activity of the Mediterranean outflow water and its interaction with the continental margin.

469 *Deep-Sea Research Part II: Topical Studies in Oceanography*, **53**, 1420–1463.

470 Hernández-Molina, F.J., Maldonado, A. and Stow, D.A.V. (2008) Abyssal plain contourites. In:

471 *Contourites. Developments in Sedimentology* (Eds Rebesco. M and A, Camerlenghi), **60**, pp.

472 379-408. Elsevier, Amsterdam.

473 Hernandez-Molina, F.J., Stow, D.A.V., Alvarez-Zarikian, C.A., Acton, G., Bahr, A., Balestra, B.,

474 Ducassou, E., Flood, R., Flores, J.A., Furota, S., Grunert, P., Hodell, D., Jimenez-Espejo, F., Kim, J.

475 K., Krissek, L., Kuroda, J., Li, B., Llave, E., Lofi, J., Lourens, L., Miller, M., Nanayama, F., Nishida,

476 N., Richter, C., Roque, C., Pereira, H., Sanchez Goni, M.F., Sierro, F.J., Singh, A.D., Sloss, C.R.,

477 Takashimizu, Y., Tzanova, A., Voelker, A., Williams, T., and Xuan, C., 2014. Onset of

478 Mediterranean outflow into the North Atlantic. *Science*, **344**, 1244-1250.

479 Hohbein, M. and Cartwright, J. (2006) 3D seismic analysis of the West Shetland Drift system:

480 Implications for Late Neogene palaeoceanography of the NE Atlantic. *Marine Geology*, **230**,

481 1-20.

482 Judd, A. G. and Hovland, M. (2007). Submarine fluid flow, the impact on geology, biology and the

483 marine environment. Cambridge University Press, 475 pp.

484 Karcher, M., Beszczynska-Möller, A., Kauker, F., Gerdes, R., Heyen, S., Rudels, B. and Schauer, U.
 485 (2011) Arctic Ocean warming and its consequences for the Denmark Strait overflow. *Journal of*
 486 *Geophysical Research C: Oceans and Atmospheres*, **116**, C02037.

487 Knutz, P.C. and Cartwright, J. (2003) Seismic stratigraphy of the West Shetland Drift: implication
 488 for late Neogene paleocirculation in the Faeroe-Shetland gateway. *Paleoceanography*, **18**,
 489 1093.

490 Laberg, J.S., Guidard, S., Mienert, J., Vorren, T.O., Haflidason, H. and Nygård, A. (2007)
 491 Morphology and morphogenesis of a high-latitude canyon; the Andøya Canyon, Norwegian
 492 Sea. *Marine Geology*, **246**, 68–85.

493 Li, S.T., Lin, C.S., Zhang, Q.M., Yang, S.G. and Wu, P.K. (1998) Dynamic process of episodic rifting
 494 in continental marginal basin and tectonic events since 10 Ma in South China Sea. *Chinese*
 495 *Science Bulletin*, **43**, 797-810.

496 Lüdmann, T., Wiggershaus, S., Betzler, C. and Hübscher, C. (2012) Southwest Mallorca Island: A
 497 cool-water carbonate margin dominated by drift deposition associated with giant mass
 498 wasting. *Marine Geology*, **307-310**, 73-87.

499 Lüdmann, T., Wong, H.K. and Berglar, K. (2005) Upward flow of North Pacific Deep Water in the
 500 northern South China Sea as deduced from the occurrence of drift sediments. *Geophysical*
 501 *Research Letters*, **32**, L05614.

502 Ma, Y.B., Wu, S.G., Lv, F.L., Dong, D.D., Sun, Q.L., Lu, Y.T. and Gu, M.F. (2010) Seismic
 503 characteristics and development of the Xisha carbonate platforms, northern margin of the
 504 South China Sea. *Journal of Asian Earth Sciences*, **40**, 770-783.

505 Masson, D.G., Wynn, R.B. and Bett, B.J. (2004) Sedimentary environment of the Faeroe- Shetland

506 Channel and Faeroe Bank channels, NE Atlantic, and the use of bedforms as indicators of
 507 bottom current velocity in the deep ocean. *Sedimentology*, **51**, 1–35.

508 Morley, C.K. (2002) A tectonic model for the Tertiary evolution of strike–slip faults and rift basins
 509 in SE Asia. *Tectonophysics*, **347**, 189–215.

510 Niemi, T.M., Ben-Avraham, Z., Hartnady, C.J.H. and Reznikov, M. (2000) Post-Eocene seismic
 511 stratigraphy of the deep ocean basin adjacent to the southeast African continental margin: a
 512 record of geostrophic bottom current systems. *Marine Geology*, **162**, 237–258.

513 Nof, D., Paldor, N. and Gorder, S. (2002) The Reddy maker. *Deep Sea Research Part I: Oceanographic Research Papers*, **49**, 1531–1549.

515 Qiu, X.L., Ye, S.Y., Wu, S.M., Shi, X.B., Zhou, D., Xia, K.Y. and Flueh, E.R. (2001) Crustal structure
 516 across the Xisha Trough, northwestern South China Sea. *Tectonophysics*, **341**, 179–193.

517 Rebesco, M. (2005) Contourites. In: *Encyclopedia of Geology* (Eds Selley, R.C., Cocks, L.R.M and
 518 I.R. Plimer), pp. 513–527. Elsevier, Oxford.

519 Rebesco, M., Hernández-Molina, F.J., Van Rooij, D. and Wåhlin, A. (2014) Contourites and
 520 associated sediments controlled by deep-water circulation processes: State-of-the-art and
 521 future considerations. *Marine Geology*, **352**, 111–154.

522 Roberts, D.G., Hogg, N.G., Derek, G., Bishop, G. and Flewellen, C.G. (1974) Sediment distribution
 523 around moated seamounts in the Rockall Trough. *Deep-Sea Research Part A: Oceanographic Research Papers*, **21**, 175–184.

525 Serra, N., Ambar, I. and Boutov, D. (2010) Surface expression of Mediterranean Water dipoles
 526 and their contribution to the shelf/slope–open ocean exchange. *Ocean Science*, **6**, 191–209.

527 Shao, L., Li, X.J., Geng, J.H., Pang, X., Lei, Y.C., Qiao, P.J., Wang, L.L. and Wang, H.B. (2007) Deep

528 water bottom current deposition in the northern South China Sea. *Science in China Series D:*
529 *Earth Sciences*, **50**, 1060–1066.

530 Stow, D.A.V., Hernández-Molina, F.J., Llave, E., Bruno, M., García, M., Díaz del Río, V., Somoza, L.
531 and Brackenridge, R.E. (2013) The Cadiz Contourite Channel: sandy contourites, bedforms and
532 dynamic current interaction. *Marine Geology*, **343**, 99-114.

533 Stow, D.A.V., Hernández-Molina, F.J., Llave, E., Sayago-Gil, M., del Río, V.D. and Branson, A. (2009)
534 Bedform-velocity matrix: The estimation of bottom current velocity from bedform
535 observations. *Geology*, **37**, 327-330.

536 Stow, D.A.V. and Johansson, M. (2000) Deep-water massive sands: nature, origin and
537 hydrocarbon implications. *Marine and Petroleum Geology*, **17**, 145-174.

538 Surlyk, F. and Lykke-Andersen, H. (2007) Contourite drifts, moats and channels in the Upper
539 Cretaceous chalk of the Danish Basin. *Sedimentology*, **54**, 405–422.

540 Sun, Q.L., Wu, S.G., Lv, F.L. and Yuan, S.Q. (2010) Polygonal faults and their implications for
541 hydrocarbon reservoirs in the southern Qiongdongnan Basin, South China Sea. *Journal*
542 *of Asian Earth Sciences*, **39**, 470-479.

543 Sun, Q.L., Wu, S.G., Cartwright, J., Lüdmann, T. and Yao, G.S. (2013) Focused fluid flow systems of
544 the Zhongjiannan Basin and Guangle Uplift, South China Sea. *Basin Research*, **25**, 97-111.

545 Sun, Q.L., Cartwright, J., Wu, S.G., Zhong, G.F., Wang, S.H. and Zhang, H.L. (2016) Submarine
546 erosional troughs in the northern South China Sea: Evidence for Early Miocene deepwater
547 circulation and paleoceanographic change. *Marine and Petroleum Geology*, **77**, 75-91.

548 Sun, Q.L., Wu, S.G., Hovland, M., Luo, P., Lu, Y.T. and Qu, T.L. (2011b) The morphologies and
549 genesis of mega-pockmarks near the Xisha Uplift, South China Sea. *Marine and Petroleum*

550 *Geology*, **28**, 1146-1156.

551 Sun, Q.L., Wu, S.G., Lüdmann, T., Wang, B. and Yang, T.T. (2011a) Geophysical evidence for cyclic

552 sediment deposition on the southern slope of Qiongdongnan Basin, South China Sea. *Marine*

553 *Geophysical Researches*, **32**, 425-428.

554 Sutherland, B., Nault, J., Yewchuck, K. and Swaters, G. (2004) Rotating dense currents on a slope.

555 Part 1. Stability. *Journal of Fluid Mechanics*, **508**, 241–264.

556 Taylor, B. and Hayes, D.E. (1983) Origin and history of the South China Sea Basin. In: *The Tectonic*

557 *and Geologic Evolution of Southeast Asian Seas and Islands 2* (Ed Hayes, D.E). 27, pp. 23–56.

558 Geophysical Monograph, American Geophysical Union.

559 Van Rooij, D., Huvenne, V.A.I., Blamart, D., Henriët, J.P., Wheeler, A. and de Haas, H. (2009) The

560 Enya mounds: a lost mound-drift competition. *International Journal of Earth Sciences*, **98**,

561 849–863.

562 Verdicchio, G. and Trincardi, F. (2006) Short-distance variability in slope bed-forms along the

563 Southwestern Adriatic Margin (Central Mediterranean). *Marine Geology*, **234**, 271–292.

564 Wang, D.W., Wu, S.G., Qin, Z.L., Spence, G. and Lv, F.L. (2013) Seismic characteristics of the

565 Huaguang mass transport deposits in the Qiongdongnan Basin, South China Sea: Implications

566 for regional tectonic activity. *Marine Geology*, **346**, 165-182.

567 Wang, P.X., Li, Q.Y. and Tian, J. (2014) Pleistocene paleoceanography of the South China Sea:

568 Progress over the past 20 years. *Marine Geology*, **352**, 381-396.

569 Xie, Q., Xiao, J.G., Wang, D.X. and Yu, Y.Q. (2013) Analysis of deep-layer and bottom circulations in

570 the South China Sea based on eight quasi-global ocean model outputs. *Chinese Science Bulletin*,

571 **58**, 1–7.

Xie, X.N., Mülle, R.D., Li, S.T., Gong, Z.S. and Steinberger, B. (2006) Origin of anomalous subsidence along the Northern South China Sea margin and its relationship to dynamic topography. *Marine and Petroleum Geology*, **23**, 745–765.

Yao, G.S., Yuan, S.Q. and Wu, S.G. (2008) The double provenance supply depositional model and its exploration prospect in the deepwater of Qiongdongnan Basin. *Petroleum Exploration and Development*, **35**, 679-685.

Yuan, D.L. (2002) A numerical study of the South China Sea deep circulation and its relation to the Luzon Strait transport. *Acta Oceanologica Sinica*, **21**, 187– 202.

Yuan, S.Q., Wu, S.G., Lüdmann, T., Yao, G.S., Lv, F.L., Cao, F., Wang, H.R. and Li, L. (2009). Fine-grained Pleistocene deepwater turbidite channel system on the slope of Qiongdongnan Basin, northern South China Sea. *Marine and Petroleum Geology*, **26**, 1441–1451.

Figure Captions

Figure 1: Sediment drift types and inferred bottom current paths. (a)-(g): Traditional drift types which are caused by steady bottom current regimes. Modified from [Rebesco \(2005\)](#), [Hernández-Molina et al. \(2008\)](#) and [Rebesco et al. \(2014\)](#). (h): New sediment drifts in the study area and the inferred bottom current paths.

Figure 2: Geological setting of the study area (red solid square, [Fig. 2a](#)) and the oceanography of northern South China Sea. The study area with complex seabed morphologies includes the southern slope of the Qiongdongnan Basin (QDNB), Guangle Massif (GLM) and the western part of Xisha Massif (XSM). Five main water exchange ways are labeled with P1 (Taiwan Strait), P2

(Luzon Strait), P3 (Mindoro Strait), P4 (Balabac Strait) and P5 (Indochina-Borneo shoal). The Northern Pacific Deep Water (NPDC) (modified from Lüdmann et al., 2005), the assumed deep-water current circulation (modified from Shao et al., 2007) and the assumed intermediate-water current circulation in the northern SCS (modified from Li et al., 2013; Chen et al., 2014) are marked with dashed lines. ZSM: Zhongsha Massif.

Figure 3: (a) Multibeam bathymetrical map of the study area. The seamount (SM) and the Xisha-Guangle Gateway (XGG) with a lot of troughs (moats), and the Main Channel (MC) are clearly observed. The locations of the 3D seismic study area (white square) is labeled; (b) Enlargement of the seamount (SM). Troughs (moats) are clearly observed at its southern and western toes; (c) Enlargement of part of honeycomb structure zone. Honeycomb structures with flat bases are circular, elliptical and polygonal in shape and separated by linear ridges; (d) Vertical profile crossing through the XGG which shows an open 'U' shape and have several troughs at its western flank; (e) Vertical profile of one circular honeycomb structure which shows its flat base. See location in (c); (f) vertical profile crosses the honeycomb structure zone and intact seabed. It shows that there is an elevation difference between these two zones. See location in (a).

Figure 4: Regional 2D seismic lines show the seismic stratigraphy of the study area. This study is focused on the shallow strata which are subdivided into four units (Unit 1: Middle Miocene; Unit 2: Late Miocene; Unit 3: Pliocene and Unit 4: Quaternary). Dark grey and light grey top bars represent compressive and extensional zones which are caused by the basement uplifts. (a) A N-S trend 2D seismic profile. The complex configuration of Unit 2 is bounded by basement highs to

the north and sediments (Unit 4) sourcing from north and onlapping onto Unit 3; (b) E-W trending 2D seismic profile. The complex seismic configurations are also bounded by basement highs to the east and west of the study area. Troughs (moats) and the Main Channel are observed. Light dark arrows represent the basement highs.

Figure 5: (a) and (b): Enlargement of part of 2D seismic profile in Fig. 4b and its line drawing. The aspect ratio is 2/3. Seismic onlaps, truncations and base laps which represent complex erosions and infills are clearly observed within Unit 2; (c) Enlargement of 2D seismic profile at the western part of the Seamount (SM). See location in Fig. 4b. Troughs (moats) with truncations can be clearly observed. The inferred bottom current flow direction is marked; (d) Line drawing of the seismic profile bounded within the black solid square in (c). The strata also show repeated erosions and infills which indicate complex current regime occurrence during sediment deposition. The inferred bottom current flow direction is marked; (e) Enlargement view of the Main Channel. See location in Fig. 4b. The Main Channel is bounded by basement highs to the east and it is filled at the top by a wedge of weak-amplitude strata interpreted as mass transported deposits.

Figure 6: (a) Interpolated seabed map of the 3D seismic study area. Honeycomb structures (Hs) and turbidity channel-levee complexes (CLCs) can be clearly observed. The honeycomb structures are characterized by circular, elliptical and polygonal shapes. The locations of Fig. 8a and Fig. 8d are labeled; (b) Detailed characteristics of a circular honeycomb structure, which shows that the structure is asymmetrical and its southwestern part is steeper.

638

639 Figure 7: 3D visualization of surfaces T20, seabed and a circular honeycomb structure. Both the
640 surfaces have honeycomb structures but the honeycomb structures at surface T20 are denser
641 and smaller. The honeycomb structures seemly originate from these at surface T20. For a single
642 honeycomb structure, it is conical shape in the three dimensions.

643

644 Figure 8: (a) A SW-NE 3D seismic profile with aspect ratio of 1/5. See location in Fig. 6. Four
645 seismic units (Unit 1 – Unit 4) and surfaces (T10 – T40) are labeled. The Unit 2 is characterized by
646 very complex seismic pattern with repeated erosions and infills and its base is characterized by a
647 lot of troughs. Unit 3 and Unit 4 display a wave-like patterns and small-scale polygonal faults can
648 be observed within Unit 1; (b) Enlargement of part of (a) with an aspect ratio of 1:1 and (c) its
649 line drawing. The repeated erosions and infills are clearly observed; (d) A SE-NW 3D seismic
650 profile with aspect ratio of 1/5. See location in Fig. 6. The sediments of Unit 4 onlap from the
651 north onto the Unit 3; (e) Enlargement of part of seismic profile from (d) with an aspect ratio of
652 1:2 and (f) its line drawing. The repeated erosions and infills are also clearly observed.

653

654 Figure 9: (a) Coherence slice of the surface T30. Most of the troughs strike NW-SE and only a few
655 show a nearly E-W trend. Honeycomb structures are much denser in the study area and it is
656 difficult to separate them in the coherence slice map. Mud diapirs are also observed; (b): 3D
657 visualization of part of surface T30. The troughs are linear and they are frequently bifurcated or
658 combined. They usually have uneven bases and slowly transfer to the honeycomb structure zone.
659 See location in (a).

660

661 Figure 10: (a) Coherence slice of part of surface T20. Linear troughs mainly trending to WNW and
662 usually associated with honeycomb structures are bifurcated or combined. The location of (b) is
663 labeled; (b) A 3D seismic profile crosscutting two troughs at surface T20. The troughs have an
664 open 'V' shape in seismic profile and are filled by sediments with onlap termination; (c) Dip slice
665 map of surface T20. The WNW-ESE troughs are dominated in the surface T20, which is different
666 from the predominated NW-SE troughs in the surface T30. The honeycomb structures are tightly
667 associated with the troughs.

668

669 Figure 11: Four coherence slice maps show the evolution of the troughs in the 3D seismic study
670 area. (a) Coherence slice of 2168 ms (TWT). It is mainly bounded within Unit 3 and the linear
671 troughs which strike NWW-SEE are located at the lower part of Unit 3 and large honeycomb
672 structures are clearly observed; (b) Coherence slice of 2368 ms (TWT). The linear troughs which
673 are located at different locations comparing with these in (a) are also observed within the lower
674 part of Unit 3; (c) and (d) include the strata of Unit 2 and upper part of Unit 1, which shows
675 similar trough characteristics at surface T30 with a dominant NW-SE and E-W orientation.

676

677 Figure 12: Structural map of T40 showing the uneven seabed morphologies. Linear anticlinal
678 structures (red pluses with cyan solid lines), isolated basement highs (red pluses), honeycomb
679 structures zone (Hs) of Unit 2 (blue dashed line), Hs zone of Unit 3 (red dashed line), Hs zone of
680 Unit 4 (yellow dashed line), Xisha Massif, Guangle Massif and Seamount (SM) are labeled. The Hs
681 zone is bounded by the linear anticlinal structures. Some isolated basement highs also develop
682 within the Hs zone, which makes the seabed more uneven.

683

Figure 13: Inferred bottom current regimes. (a) Present bottom current regimes. Bottom currents reach to the study area through the region between the Guangle Massif and the Xisha Massif; (b) Early Pliocene bottom current regimes. It had a similar flow pattern to the present bottom current circulation. But a weak bottom current flowing from the west was possibly also active in the study area in the Early Pliocene. QDNB: Qiongdongnan Basin; Hs: Honeycomb Structures. The study area and inferred flow directions are marked with black square and dashed pink lines, respectively.

Figure 14: Skeleton map showing the main seabed and underlying structures and bottom current regimes in the study area. Steady bottom currents flow downslope and become unsteady when they meet the complex seabed morphologies. See text for details.

696 Table caption

697 Table 1: Geomorphologic characteristics of honeycomb structures, Main Channel and troughs in
 698 the study area. W. = width; A. = area; D. = depth; L. = length.

699

Geomorphologies		W./km	A./km ²	D./m	L./km	Shapes	Directions
Honeycomb structures		0.77-4.4	0.57-6.48 (AA. 2.6)	9-58		circular, elliptical, polygonal	
Main channel		2.00-5.00		150-250	>100	linear	NW-SE
Troughs	Seabed				10-25	linear	Parallel to the slope of SMs
	Surface T20	0.50-1.00		50-110		Linear to slightly sinuous	NW-SE
	Surface T30	0.50-2.00		10s-250	10-30	linear	NW-SE or W-E

700

Figure 1

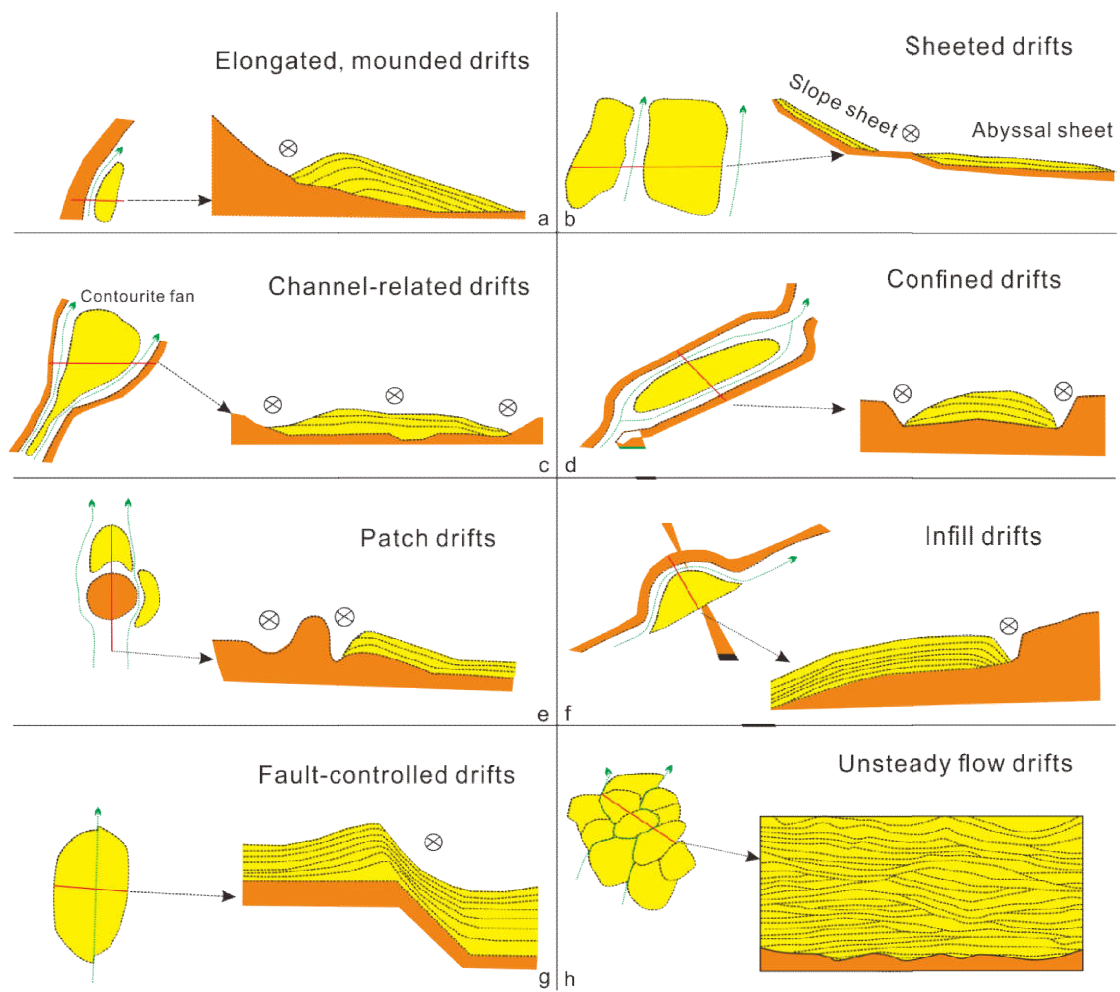


Figure 2

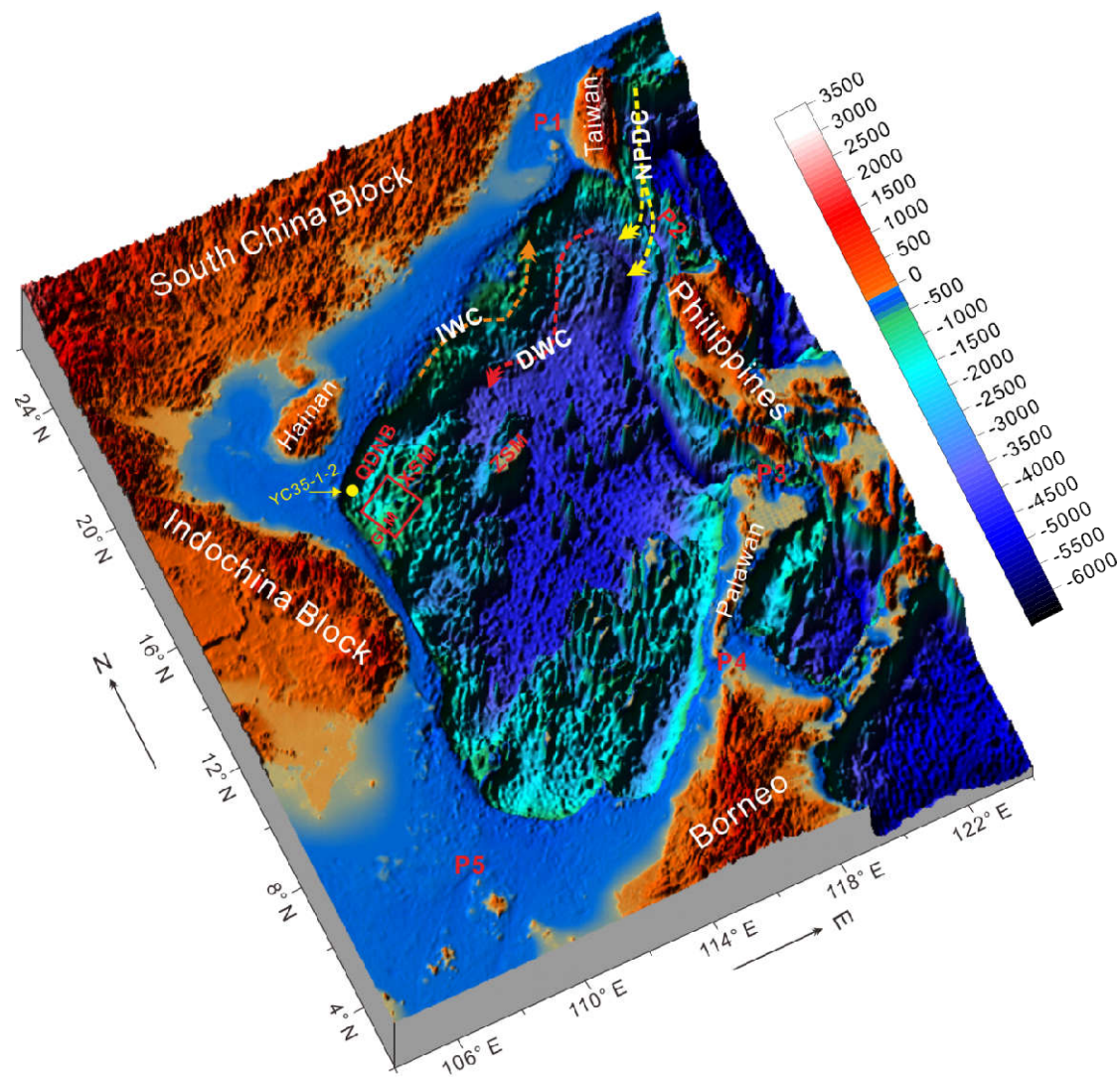


Figure 3

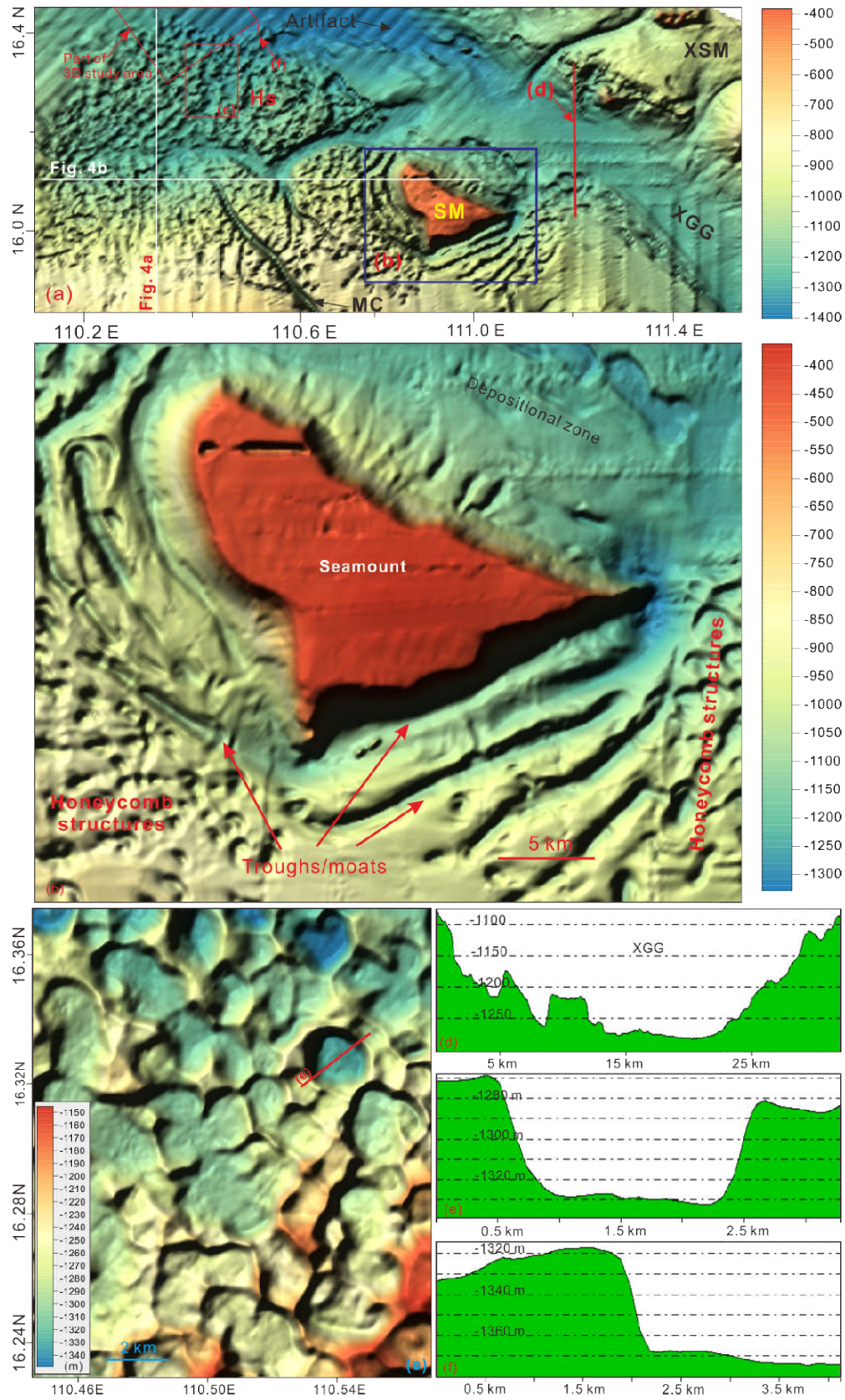


Figure 4

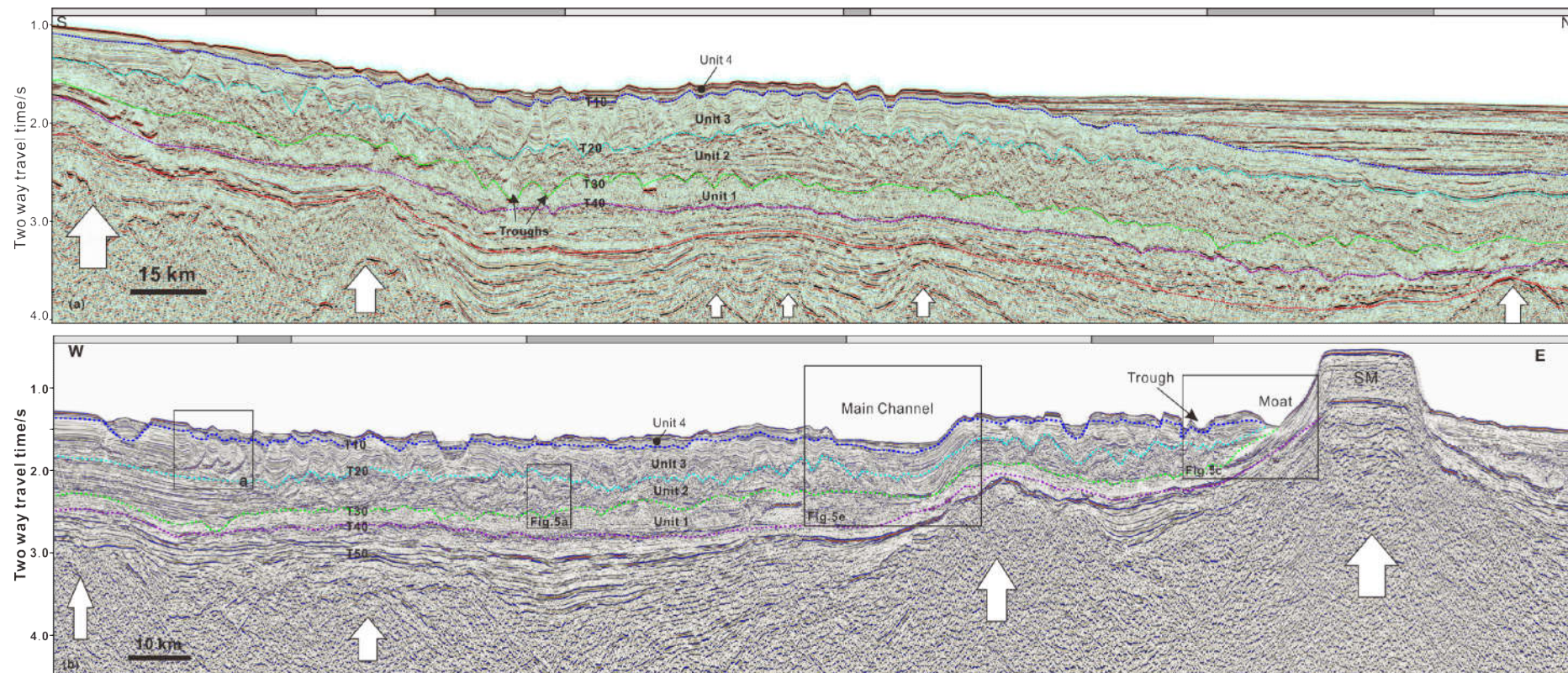


Figure 5

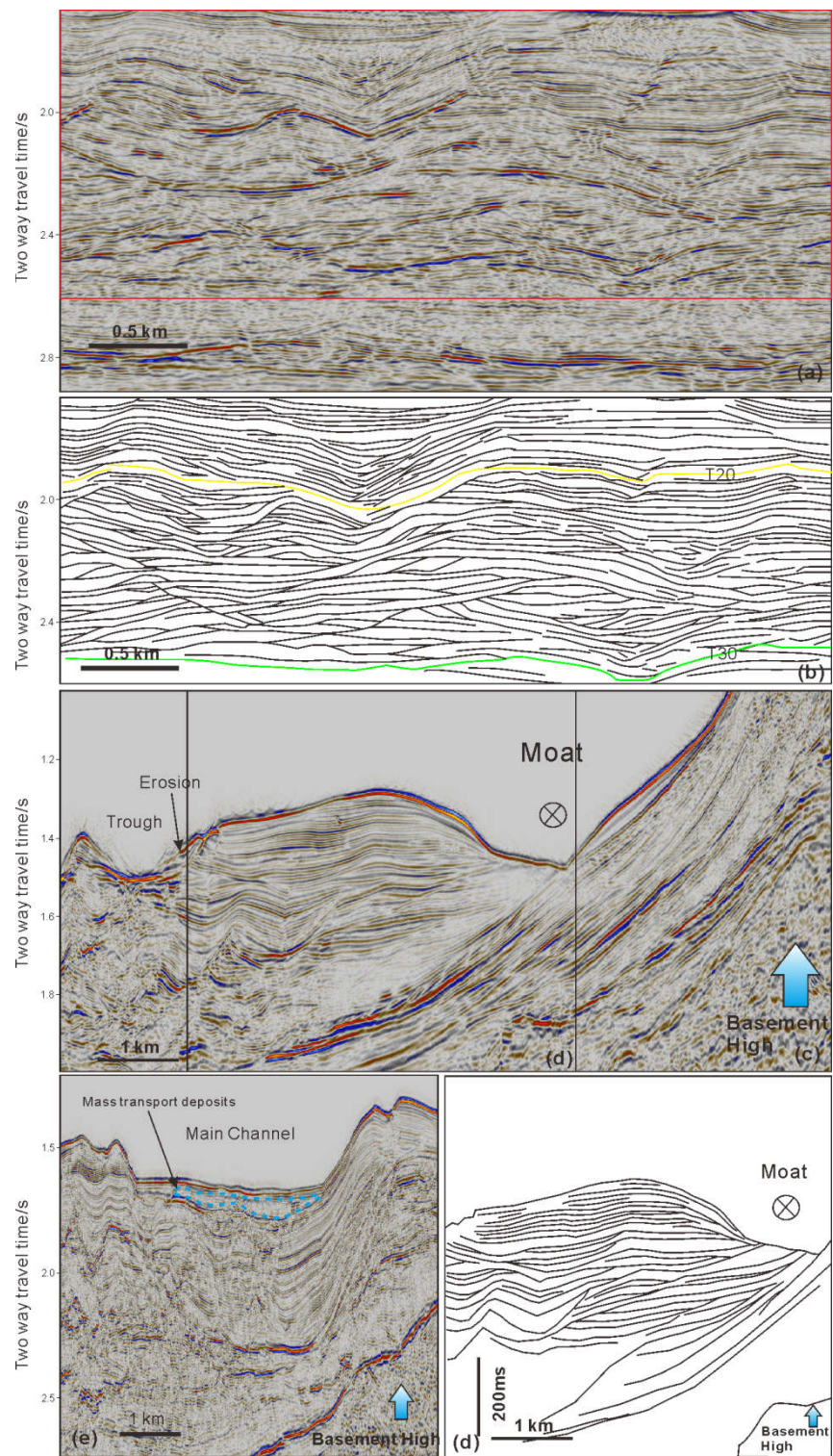


Figure 6

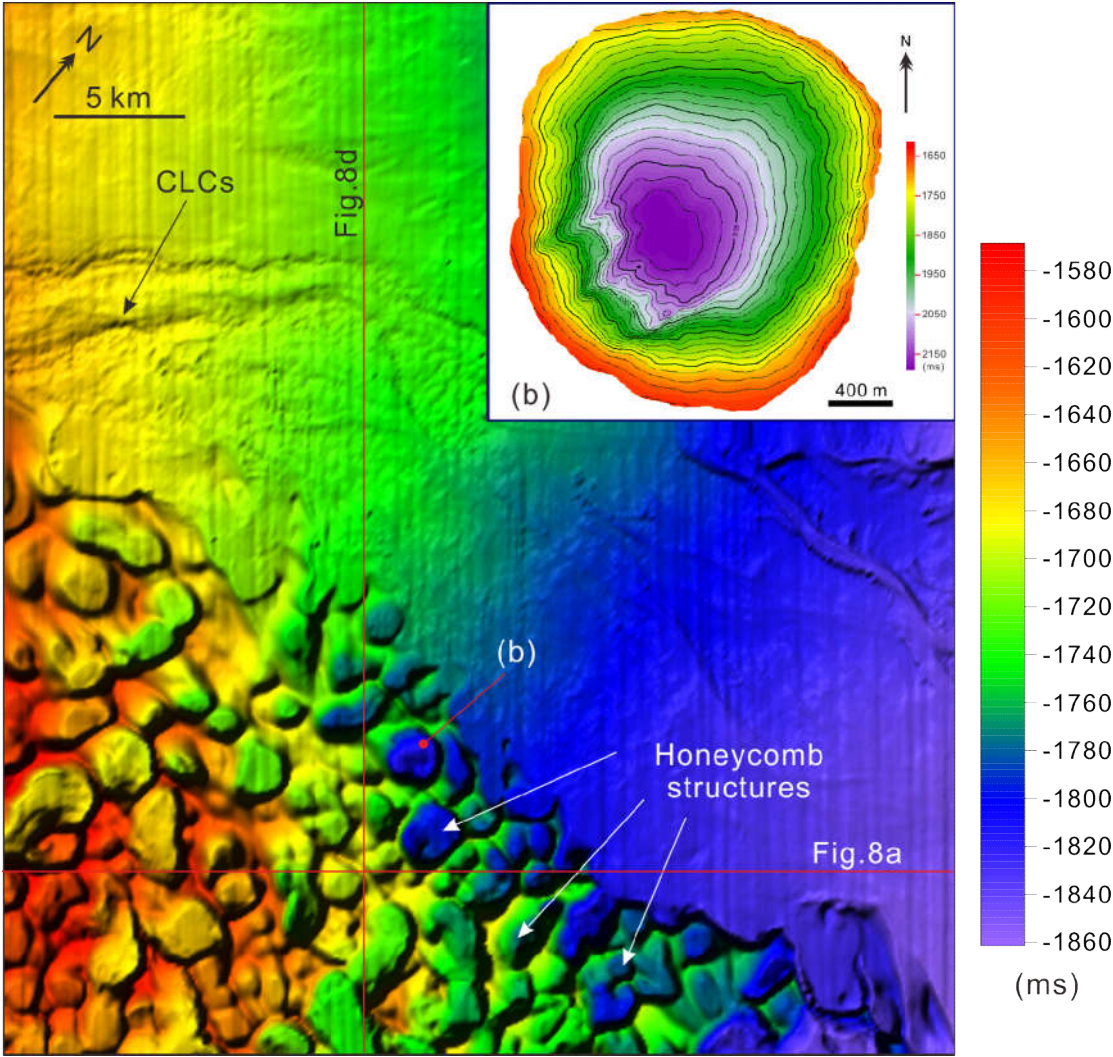


Figure 7

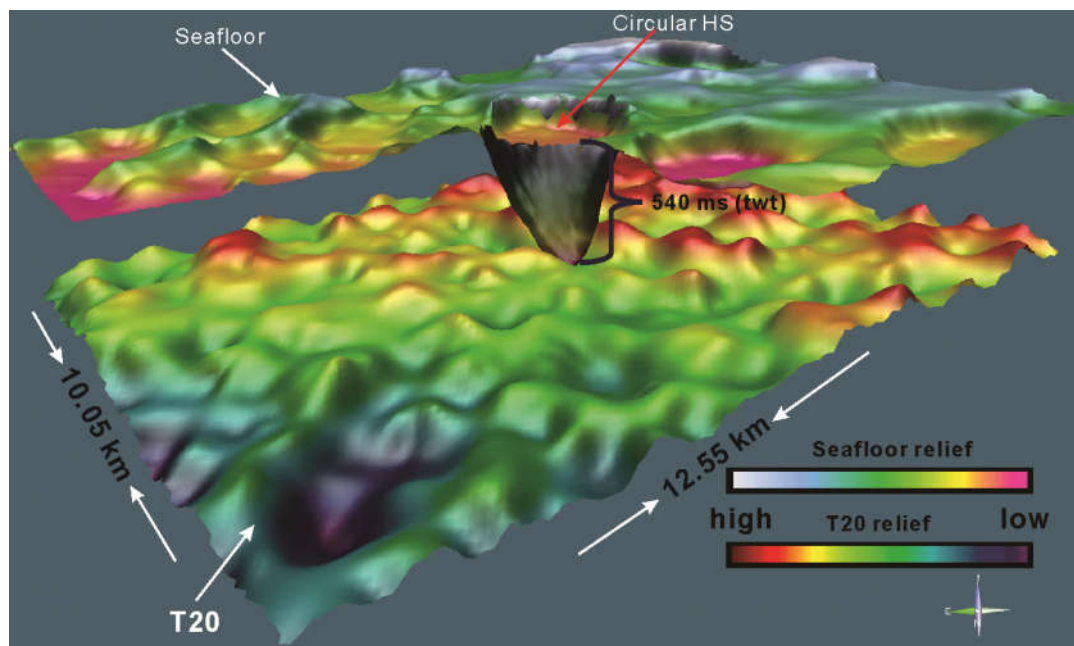


Figure 8

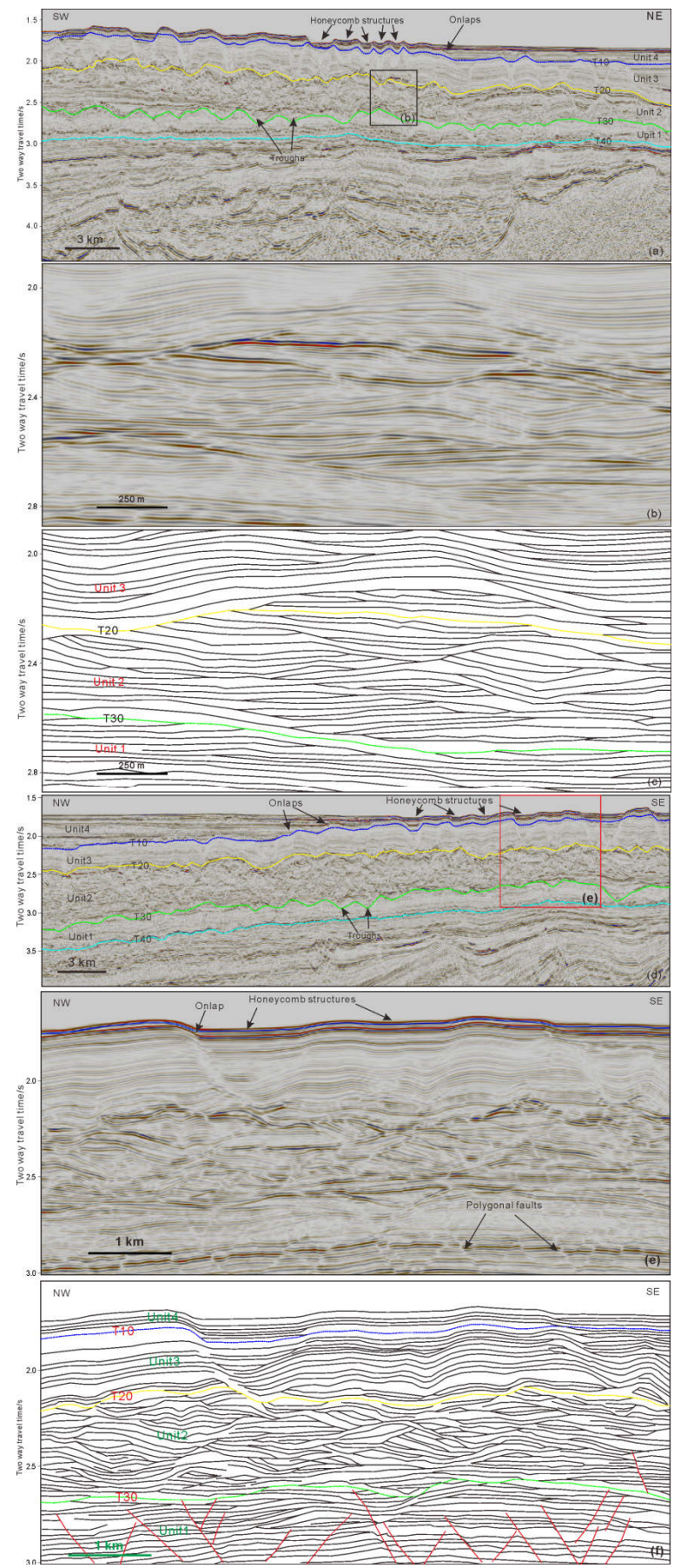


Figure 9

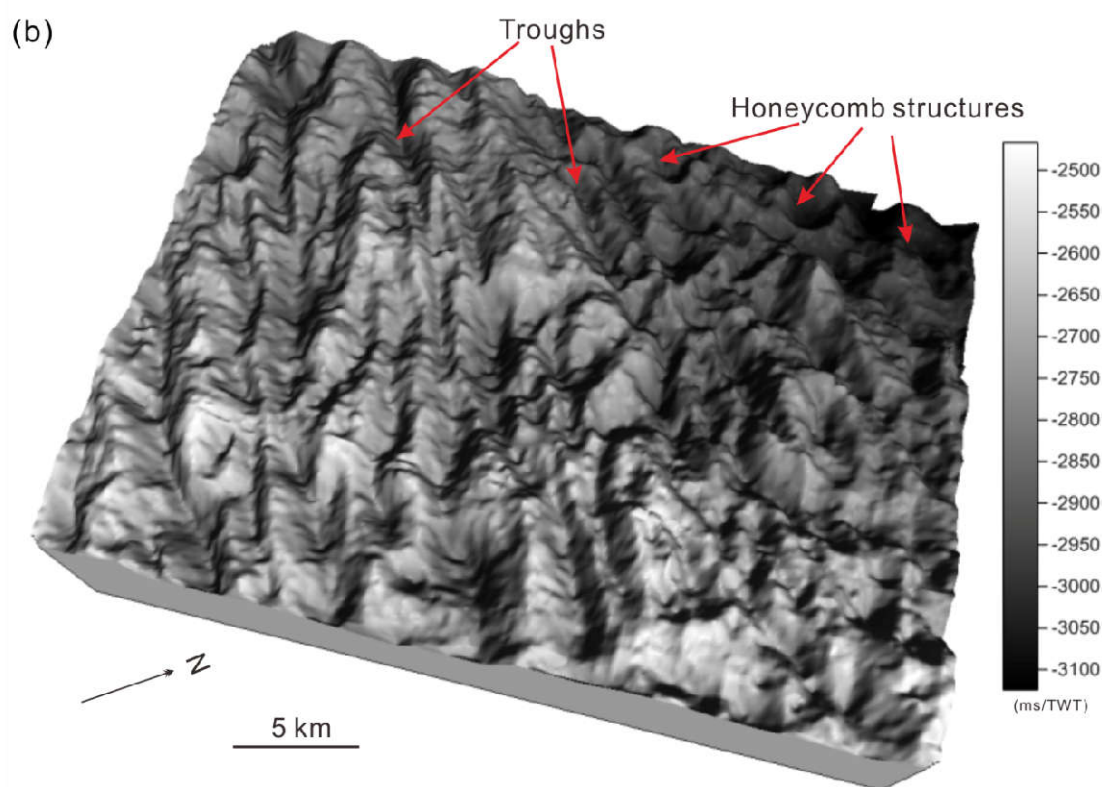
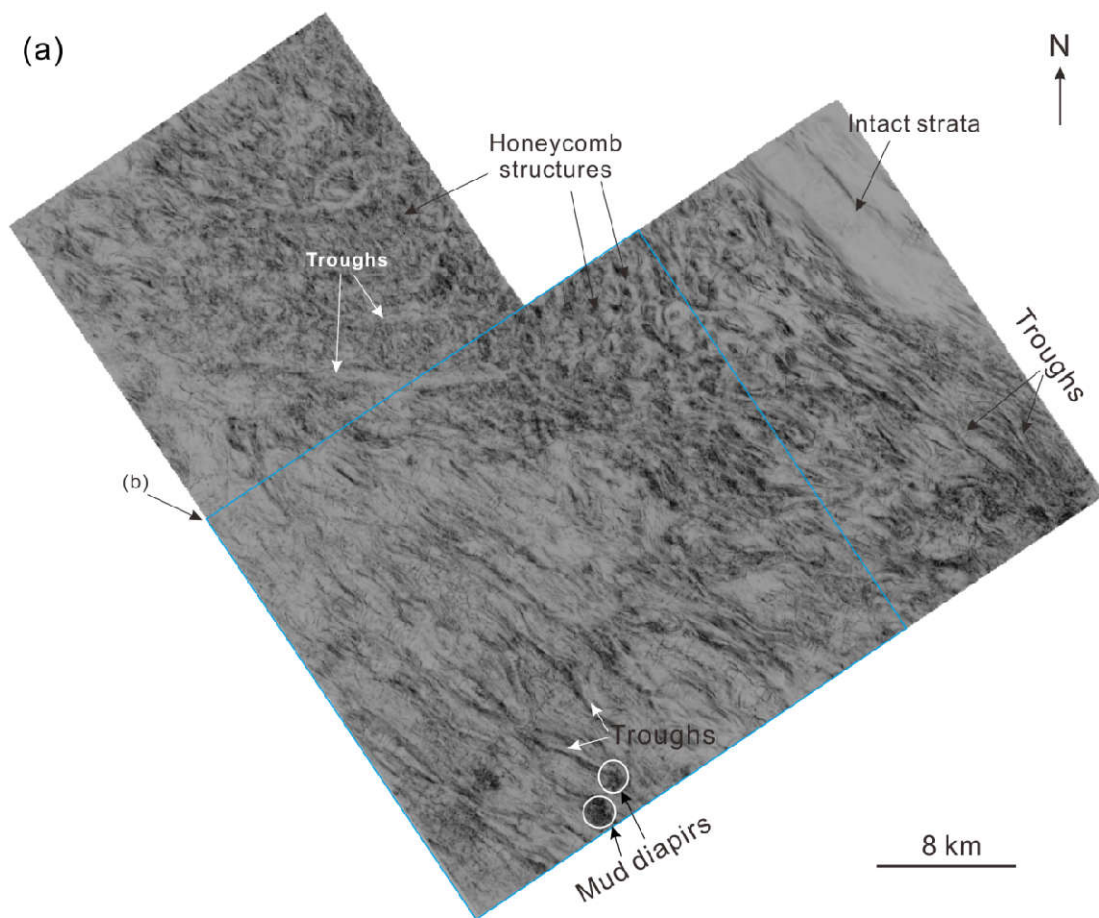


Figure 10

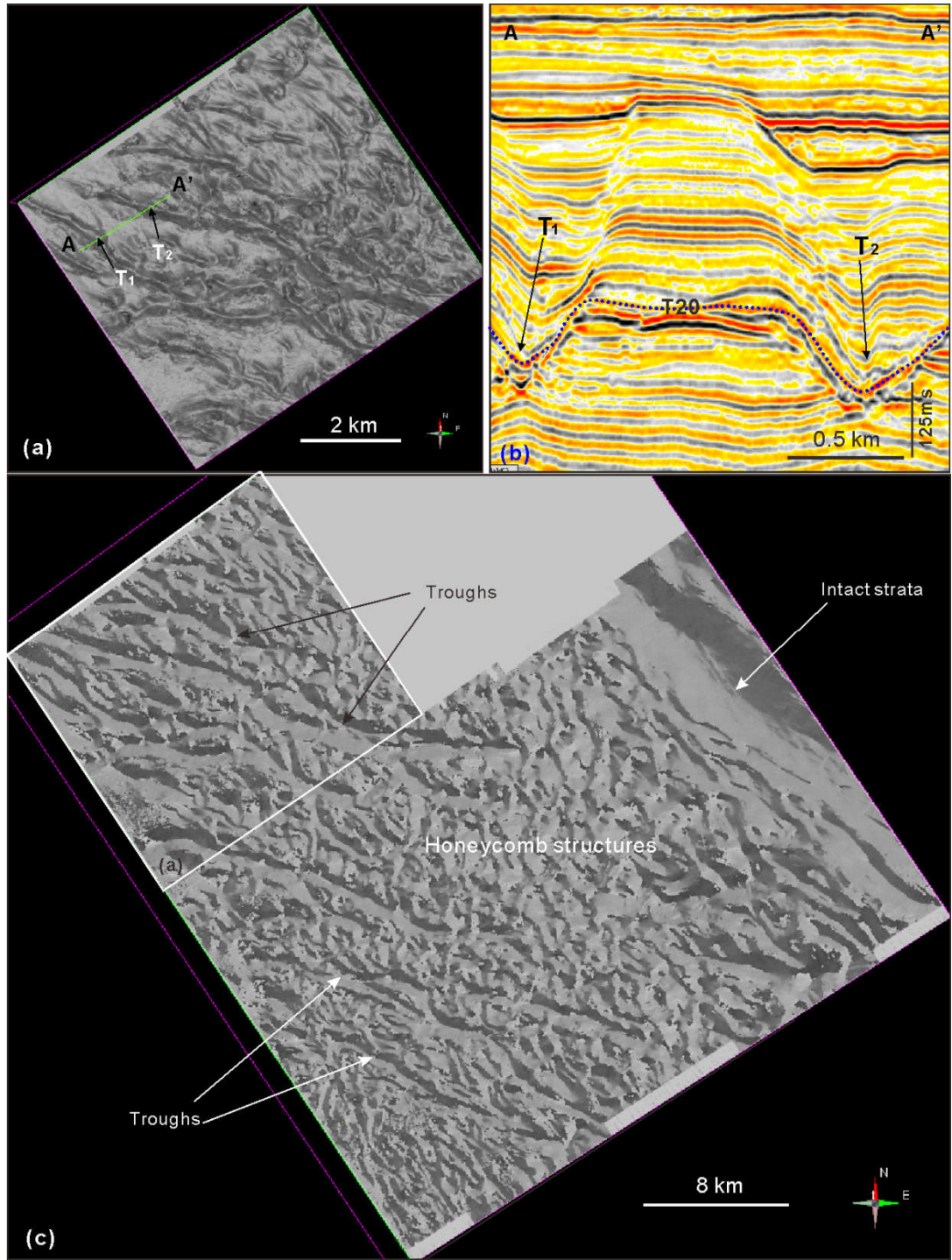


Figure 11

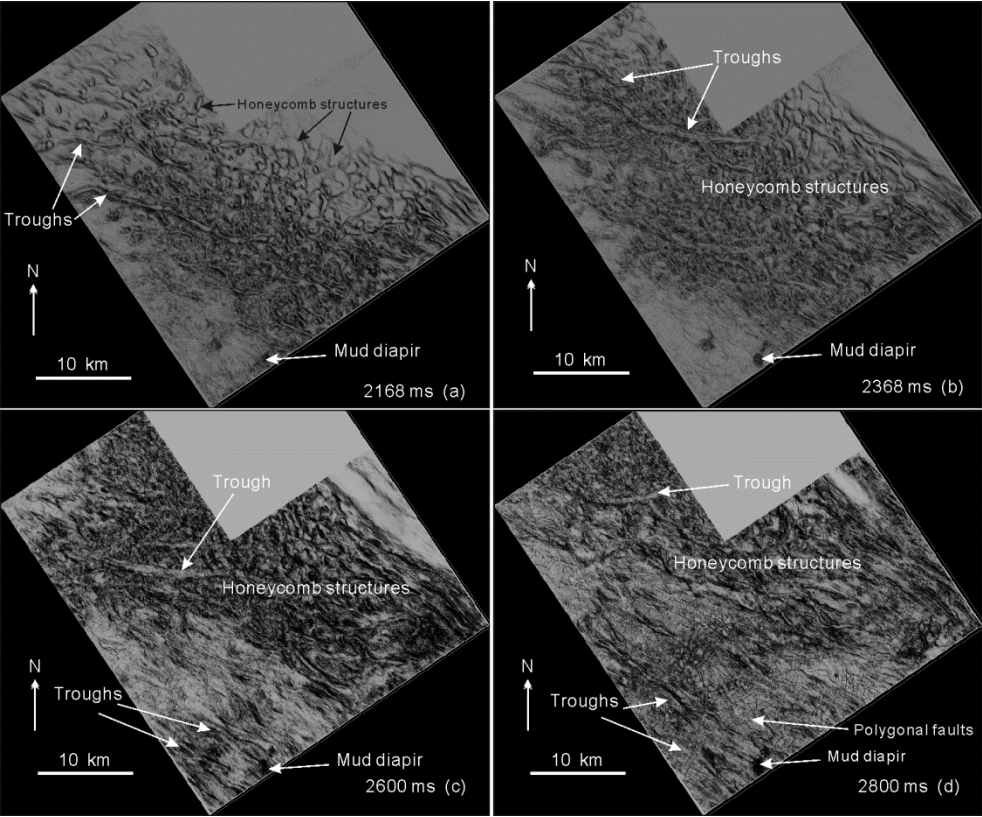


Figure 12

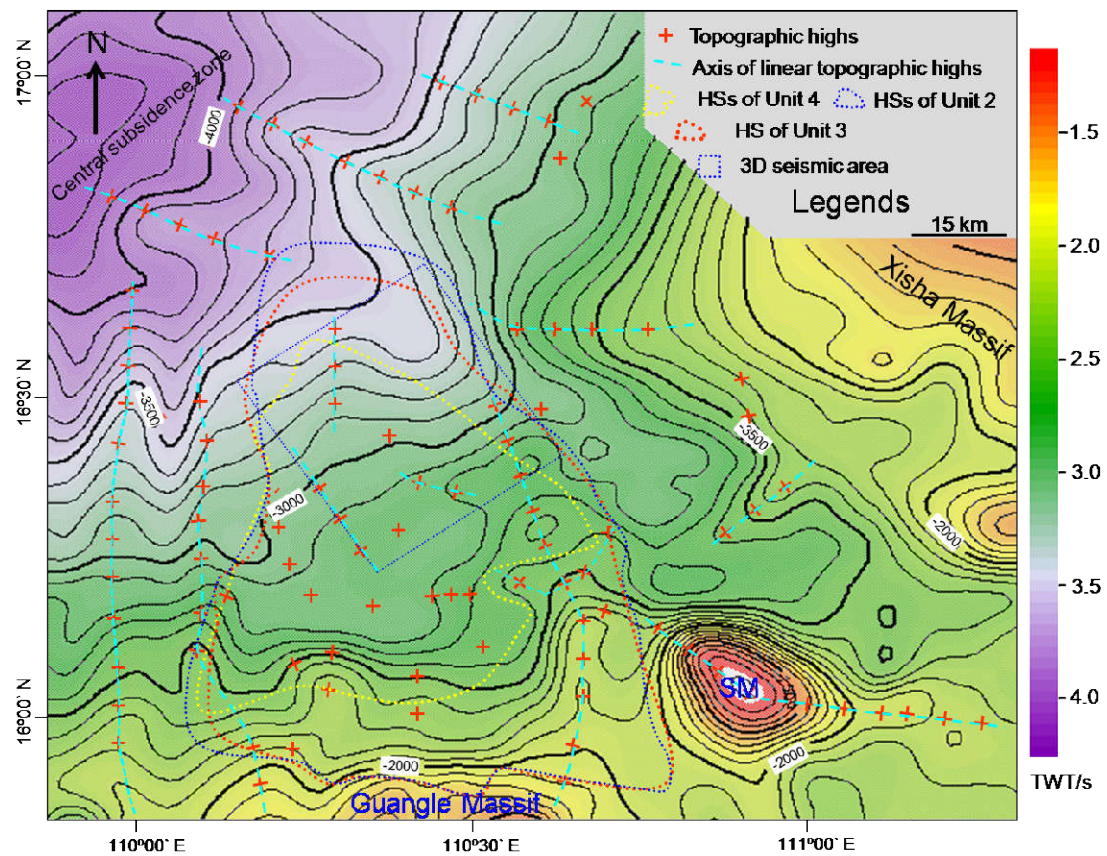


Figure 13

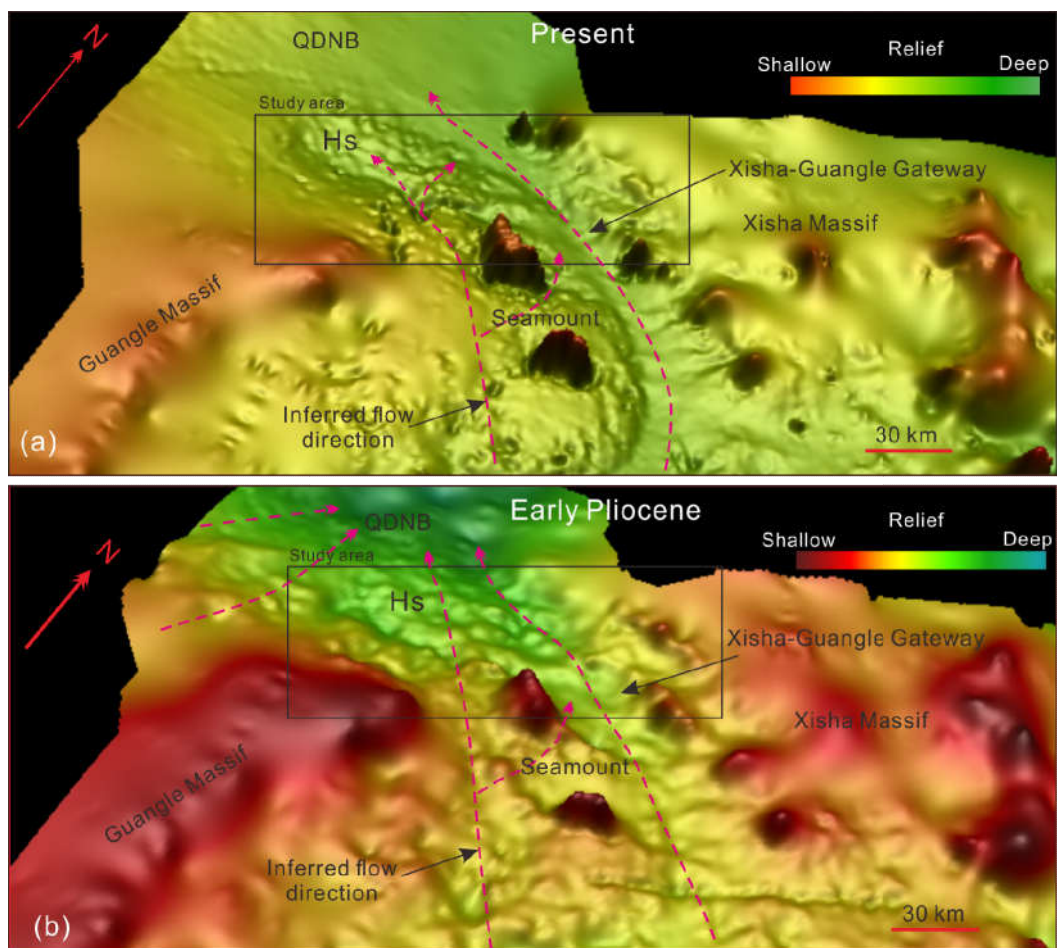


Figure 14

